Available online at www.sciencedirect.com

ScienceDirect

Acta Materialia 62 (2014) 258–266

Acta MATERIALIA

www.elsevier.com/locate/actamat

Bismuth titanate nanobelts through a low-temperature nanoscale solid-state reaction

Pin Hao [a], Zhenhuan Zhao [a], Jian Tian [a], Yuanhua Sang [a], Guangwei Yu [a], Hong Liu [a,b,*], Shaowei Chen [c,*], Weijia Zhou [d]

[a] State Key Laboratory of Crystal Materials, Shandong University, Jinan, Shandong 250100, People's Republic of China
[b] Beijing Institute of Nanoenergy and Nanosystems, Chinese Academy of Sciences, Beijing 100864, People's Republic of China
[c] Department of Chemistry and Biochemistry, University of California, 1156 High Street, Santa Cruz, CA 95064, USA
[d] New Energy Research Center, College of Environment and Energy, South China University of Technology, Guangzhou Higher Education Mega Center, Guangzhou, Guangdong 510006, People's Republic of China

Received 23 July 2013; received in revised form 1 October 2013; accepted 4 October 2013
Available online 30 October 2013

Abstract

In this study, an effective low-temperature method was developed, for the first time, for the synthesis of bismuth titanate nanobelts by using $Na_2Ti_3O_7$ nanobelts as the reactants and templates. The experimental procedure was based on ion substitution followed by a nanoscale solid-state reaction. In the first step, $Na_2Ti_3O_7$ nanobelts were soaked in a bismuth nitrate solution where ion substitution at the nanobelt surfaces led to the formation of a bismuth compound overlayer. The resulting bismuth-modified nanobelts were then subject to a calcination process at controlled temperatures. At the calcination temperature of 400 °C, the top layer was converted to Bi_2O_3 whereas the interior was converted to TiO_2(B), forming TiO_2(B)@Bi_2O_3 core–shell nanobelts. When the calcination temperature was increased to 450 °C, a metastable interphase $Bi_{20}TiO_{32}$ was produced on the nanobelt surface whereas the interior structure remained virtually unchanged, and the nanobelts now exhibited a TiO_2(B)@$Bi_{20}TiO_{32}$ core–shell structure. At calcination temperatures higher than 550 °C, the shell of the nanobelts became $Bi_4Ti_3O_{12}$. At even higher temperatures (600–700 °C), no TiO_2(B) was found and the nanobelts exhibited single-crystalline characteristics that were consistent with those of $Bi_4Ti_3O_{12}$. Such a structural evolution was manifested in X-ray diffraction, Raman and Fourier transform infrared spectroscopic measurements, and scanning electron microscopic and transmission electron microscopic studies showed that the belt-like surface morphology was maintained without any apparent distortion or destruction. A mechanism based on nanoscale solid-state reactions was proposed to account for the structural evolution. Photoluminescence measurements showed that the core–shell nanobelts exhibited a markedly suppressed emission intensity, suggesting impeded recombination of photogenerated carriers as compared to the single-phase counterparts. Such a unique feature was found to be beneficiary to photocatalysis, as exemplified by the photodegradation of methyl orange under UV irradiation, where TiO_2(B)@$Bi_{20}TiO_{32}$ core–shell nanobelts were found to exhibit the best performance among the series.

Keywords: Bismuth titanate nanobelts; Solid-state reaction; Template; Photocatalysis; Methyl orange

1. Introduction

In recent decades, Bi-based titanates have been extensively studied because of their potential applications as photorefractive materials, ferroelectric materials, capacitors, dielectric materials, actuators and photocatalysts [1–4]. Bismuth titanates include a very large family of different chemical compositions, such as $Bi_2Ti_2O_7$, $Bi_2Ti_4O_{11}$, $Bi_4Ti_3O_{12}$, $Bi_{12}TiO_{20}$, and $Bi_{20}TiO_{32}$ [5]. Among these, $Bi_{20}TiO_{32}$, with a band gap of ca. 2.38 eV, displays the highest photocatalytic activity due to the hybridized valence band (VB) by Bi6*s* and O2*p* orbitals [6]. Recently,

* Corresponding authors. Tel.: +1 8314595841; fax: +1 8314592935.
E-mail addresses: hongliu@sdu.edu.cn (H. Liu), shaowei@ucsc.edu (S. Chen).

1359-6454/$36.00
http://dx.doi.org/10.1016/j.actamat.2013.10.006

a number of methods have been reported for the preparation of crystalline bismuth-based titanates, including solid-state [7], sol–gel [8,9] and hydrothermal methods [10]. For instance, Cheng et al. [6] reported the synthesis of granular $Bi_{20}TiO_{32}$ nanoparticles through the melting of oxide precursors at 1000 °C, followed by quenching process at room temperature. In this procedure, $Bi_{20}TiO_{32}$ was formed as a metastable phase. In another study, by Yao et al. [11], granular $Bi_4Ti_3O_{12}$ nanoparticles were fabricated using metal–organic polymeric precursors, which showed good photocatalytic properties. It should be noted that the bismuth titanates reported in most early studies are in granular forms in which the abundant barriers of charge transport limit the photocatalytic performance. Furthermore, the nanoparticles are difficult to recycle, which limits their practical applications in continuous filtering photocatalytic devices.

In contrast, photocatalysts with a nanobelt morphology may provide efficient pathways for charge transport and hence reduce the rates of charge carrier recombination as compared to other nanostructures [12]. In addition, the high specific surface area of nanobelts may offer abundant active sites for the assembly of secondary phase particles to form nanoscale heterostructures with Schottky, p-n and band matching effects [13–20], so as to improve the photocatalytic performance as a result of the diminishment of photo-induced carrier recombination, the enlargement of light active facets and widening of the light absorption range [21]. Most importantly, nanobelts may be assembled into paper-like membranes [22] and exploited for continuous photocatalysis [23]. Therefore, it is of both fundamental and technological significance to develop effective protocols for the preparation of one-dimensional bismuth titanates. Nevertheless, whereas bismuth titanates have been prepared in the forms of nanospheres, nanosheets and nanocones [24,25], reports for the synthesis of bismuth titanate nanobelts have been scarce [26]. In fact, pure belt-like $Bi_{20}TiO_{32}$ and $Bi_4Ti_3O_{12}$, with lengths of several tens of micrometers, have not been reported until now.

Herein, for the first time ever, we report a facile approach to the synthesis of bismuth titanate nanobelts through a solid-state reaction by using $Na_2Ti_3O_7$ nanobelts as the reactants and templates. In this procedure, $H_2Ti_3O_7$@$BiONO_3$ nanobelts were first synthesized by the immersion of $Na_2Ti_3O_7$ nanobelts into a bismuth nitrate solution, which were then subject to a calcination process at controlled temperatures. At low temperatures (e.g. 400 °C), a TiO_2(B)@Bi_2O_3 core–shell structure was formed; when the calcination temperature was increased to 450 °C, the shell was transformed into $Bi_{20}TiO_{32}$ on the surface of the TiO_2(B) nanobelts. With a further increase in the calcination temperature (600–700 °C), single-crystalline $Bi_4Ti_3O_{12}$ nanobelts were produced as the final products most probably through a nanoscale solid-state reaction between the Bi_2O_3 shell and the TiO_2(B) core. The photocatalytic activity of the three kinds of TiO_2-based nanobelts, TiO_2(B)@Bi_2O_3, TiO_2(B)@$Bi_{20}TiO_{32}$ and $Bi_4Ti_3O_{12}$, demonstrated that the core–shell nanobelts possess much enhanced UV photocatalytic activity, as exemplified by the photodegradation of methyl orange, in comparison with that of the single-crystalline $Bi_4Ti_3O_{12}$ nanobelts. This was accounted for by the reduced recombination of photogenerated carriers in the core–shell nanobelts.

2. Experimental section

2.1. Materials

Analytic grade sodium hydroxide (NaOH) and bismuth nitrate ($Bi(NO_3)_3{\cdot}5H_2O$) were used directly, without further purification. Titania P25 (TiO_2; ca. 80% anatase and 20% rutile) was used as the titanium source to prepare $Na_2Ti_3O_7$ nanobelts. Deionized water was used throughout the experiments.

2.2. Preparation of $Na_2Ti_3O_7$ and TiO_2(B) nanobelts

$Na_2Ti_3O_7$ nanobelts were prepared by an alkaline hydrothermal process, as detailed in our previous study [27]. In a typical procedure, 0.30 g of commercial TiO_2 powder (P25) was dispersed in 60 ml of a 10 M NaOH aqueous solution, which was then placed in an 80 ml Teflon-lined autoclave. The autoclave was heated to and maintained at 200 °C for 72 h. The precipitate was collected and washed thoroughly with deionized water, affording $Na_2Ti_3O_7$ nanobelts.

To prepare TiO_2(B) nanobelts, $Na_2Ti_3O_7$ nanobelts were immersed in a 0.1 M HCl aqueous solution for 24 h and washed thoroughly with distilled water to obtain $H_2Ti_3O_7$ nanobelts, which were then annealed at 400 °C for 4 h to afford TiO_2(B) nanobelts [27].

2.3. Preparation of bismuth titanate nanobelts

Bismuth-modified titanate nanobelts were prepared by using the $Na_2Ti_3O_7$ nanobelts obtained above as the templates. In brief, 2.425 g of $Bi(NO_3)_3{\cdot}5H_2O$ was added to 200 ml of deionized water, followed by ultrasonification and magnetic stirring for 30 min to obtain a suspension. Next, 0.3775 g of $Na_2Ti_3O_7$ nanobelts was added to the above solution. The mixture was ultrasonicated for 10 min and gently stirred for another 30 min. The white precipitates were collected by filtration, washed with deionized water and then dried at 70 °C. Finally, the precipitates were annealed in air at 400, 450, 550 and 600 °C for 2 h to obtain TiO_2(B)@Bi_2O_3, TiO_2(B)@$Bi_{20}TiO_{32}$, TiO_2(B)@$Bi_4Ti_3O_{12}$ and $Bi_4Ti_3O_{12}$ nanobelts, respectively.

2.4. Preparation of $BiONO_3$ nanoparticles

In brief, 2.425 g of $Bi(NO_3)_3{\cdot}5H_2O$ was added to 200 ml of deionized water, followed by ultrasonification and magnetic stirring for 30 min. The white precipitates were

collected by filtration, washed with deionized water and then dried at 70 °C.

2.5. Characterization

The X-ray powder diffraction (XRD) patterns of the nanobelts were recorded on a Bruker D8 Advance powder X-ray diffractometer with Cu Kα radiation ($\lambda = 0.15406$ nm) over a 2θ scan range of 15–80°. Raman spectra were acquired with a Jobin–Yvon HR 800 spectrometer. Fourier transform infrared (FTIR) spectra were obtained using a NEXUS 670 FTIR spectrometer (Thermo Nicolet Co.). A HITACHI S-4800 field-emission scanning electron microscope (FE-SEM) was used to characterize the morphology and size of the catalysts. High-resolution transmission electron microscopic (HRTEM) images were obtained with a JEOL JEM 2100F microscope. UV–vis diffuse reflectance spectroscopic (DRS) measurements were carried out using a Shimadzu UV 2550 spectrophotometer with an integrating sphere attachment. $BaSO_4$ was used as the reflectance standard, and the wavelength range was 200–800 nm. Photoluminescence (PL) spectra were recorded using a FLS920 fluorescence spectrometer with an excitation wavelength of 300 nm. The concentrations of Na^+ ions in the nanobelt suspensions were measured using an X Series ICP-AES (Thermo Fisher Scientific, USA). The zeta potentials of the $BiONO_3$ and $H_2Ti_3O_7$ suspensions were measured sing a Brookhaven zeta potential analyzer.

2.6. Photocatalysis

Methyl orange (MO), a well-known acid–base indicator, was used as a model pollutant. In a typical experiment, 20 ml of an MO aqueous solution at a concentration of 20 mg l^{-1} and 20 mg of the nanobelt catalysts prepared above were placed in a quartz reactor. Before illumination, the suspension was magnetically stirred in the dark for 30 min to establish an adsorption/desorption equilibrium between MO and the surface of the photocatalysts. The photocatalytic reactions were carried out at room temperature. A 300 W mercury lamp with a primary wavelength of 365 nm was used as the UV light source. At different illumination time intervals, the mixture was centrifuged to remove the catalyst particles and an aliquot of the supernatant solution was sampled for analysis where the concentration of MO was quantified with a UV–vis spectrophotometer (UV-2102PC) by monitoring the absorbance at 465 nm.

3. Results and discussion

Fig. 1 shows the XRD profiles of the bismuth-modified titanate nanobelts prepared at different calcination temperatures. The initial $Na_2Ti_3O_7$ nanobelts were well crystallized (Fig. S1 in the Electronic Supplementary Information), and no additional diffraction patterns were

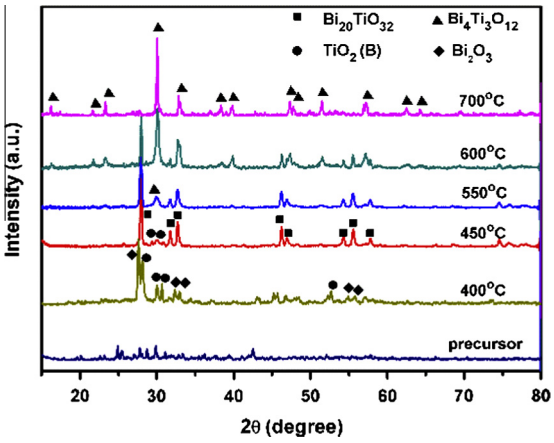

Fig. 1. XRD patterns of hybrid nanobelts calcined at different temperatures.

observed with the Bi-modified $Na_2Ti_3O_7$ precursor nanobelts prior to thermal annealing, indicating that the nanobelts likely included an amorphous bismuth-based compound layer on the surface. After thermal annealing at 400 °C, several well-defined diffraction peaks emerged at 27.9°, 30.2°, and 30.6° (filled diamonds) and at 29.70°, 29.94°, and 30.68° (filled circles), which may be indexed to Bi_2O_3 (JCPDS file No. 50-1008) and TiO_2(B) (JCPDS file No. 46-1237), respectively, indicating the formation of triclinic Bi_2O_3 and TiO_2(B). At the calcination temperature of 450 °C, whereas the diffraction features of TiO_2(B) remained unchanged, the peaks of Bi_2O_3 disappeared, and new features appeared at 28.02°, 31.62°, 32.88°, 46.26°, 47.18°, 54.16°, 55.77°, 57.91°, 74.61°, and 75.94° (filled squares), which may be assigned to the (201), (002), (220), (222), (400), (203), (421), (402), (423) and (601) planes of tetragonal $Bi_{20}TiO_{32}$ (JCPDS file No. 42-0202), respectively. This indicated that, at this temperature, the Bi_2O_3 layer was converted into $Bi_{20}TiO_{32}$. For the samples annealed at 550 °C, a new diffraction peak emerged at 30° (filled triangle) which can be indexed to orthorhombic $Bi_4Ti_3O_{12}$ (JCPDS file No. 50-0300). With a further increase in the calcination temperature, the diffraction peaks become sharper with enhanced intensity, indicating an increase in the $Bi_4Ti_3O_{12}$ content. After calcination at 700 °C, all the XRD peaks of the samples could be indexed to orthorhombic $Bi_4Ti_3O_{12}$ with a layered perovskite structure. No peaks from other phases were detected, indicating the high purity of the products. From these measurements, it can be seen that the $Bi_{20}TiO_{32}$ was formed as a metastable interphase between TiO_2(B)@Bi_2O_3 and $Bi_4Ti_3O_{12}$.

Raman spectroscopic measurements further confirmed the formation of metastable $Bi_{20}TiO_{32}$ in the hybrid nanobelt sample when calcined at 450 °C. TiO_2(B) nanobelts synthesized by calcining $H_2Ti_3O_7$ was used as a reference. The Raman spectra of the two samples are shown in Fig. 2. The typical vibrational bands of TiO_2(B) can be found at 123, 237 and 248 cm^{-1}, while the bands at around

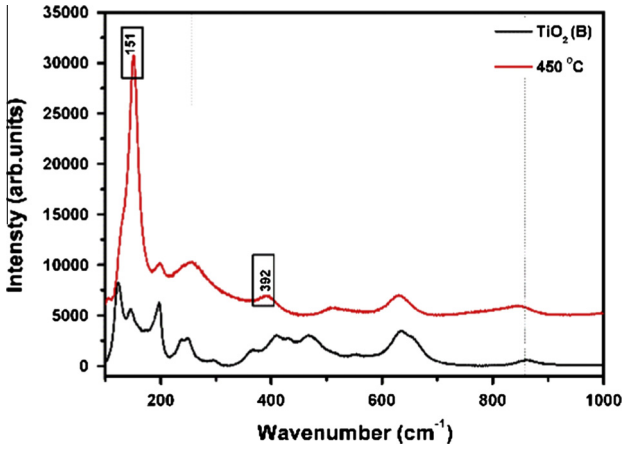

Fig. 2. Raman spectra of TiO_2(B) (black curve) and $Bi_{20}TiO_{32}$ nanobelts (red curve) that were prepared by calcination of Bi-modified titanate nanobelts at 450 °C. (For interpretation of the references to color in this figure legend, the reader is referred to the web version of this article.)

145, 197 and 632 cm^{-1} are attributed to the E_g vibrations of anatase TiO_2 [28]. The spectrum of the sample sintered at 450 °C is similar to that of TiO_2(B), indicating the existence of TiO_2(B) nanobelts as a backbone in the hybrid nanobelts. However, two new vibration features emerged at 151 and 392 cm^{-1} that were consistent with those of $Bi_{20}TiO_{32}$ [28]. This indicates that Bi_2O_3 on the TiO_2(B) surface likely reacted with the interior TiO_2(B) to form $Bi_{20}TiO_{32}$ at 450 °C, as suggested in the above XRD measurements (Fig. 1).

The phase transformation of the bismuth titanate nanobelts was also examined by FTIR measurements. Fig. 3 shows the infrared spectra of the samples prepared at different calcination temperatures. The peaks around 1575 cm^{-1} can be ascribed to the bending mode of absorbed water (δ_{OH}) [29]. The peak around 470 cm^{-1} is likely caused by the O–Ti–O stretching vibration of TiO_2(B). With an increase in the annealing temperature from 450 to 700 °C, the intensity of this peak deceases,

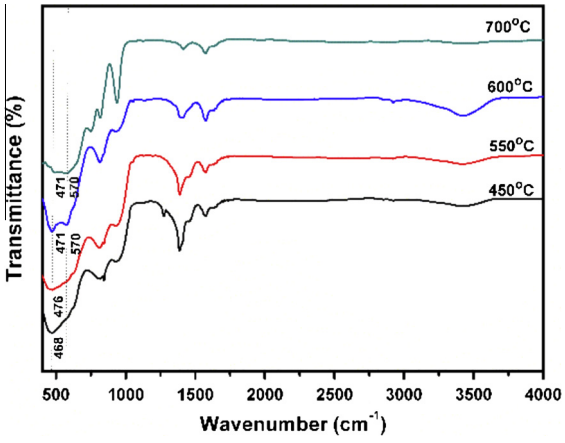

Fig. 3. FTIR spectra of hybrid nanobelts prepared by calcination at different temperatures.

suggesting a diminution of the TiO_2(B) content. Meanwhile, the peak around 570 cm^{-1} started to appear at 600 and 700 °C, which is characteristic of $Bi_4Ti_3O_{12}$ [30]. Taken together, the FTIR results are consistent with the XRD and Raman data presented above.

The morphologies of the various nanobelts were then studied by SEM measurements. Fig. 4 depicts the SEM images of the Bi-modified nanobelts (a) before and after calcination at (b) 450 °C, (c) 600 °C and (d) 700 °C. From panel (a) of the initial (uncalcined) Bi-modified nanobelts, belt-like one-dimensional nanostructures can be clearly seen, similar to those of the $Na_2Ti_3O_7$ nanobelts that functioned as reactants and templates in the synthesis (Fig. S2a). The Bi-modified nanobelts were rather uniform, being 30–50 nm in thickness, 150–300 nm in width and up to several tens of micrometers in length. The nanobelts also exhibited smooth surfaces that were decorated with small nanoparticles. Note that the width and thickness are slightly greater than those of the $Na_2Ti_3O_7$ nanobelts. This was probably due to the formation of a bismuth compound overlayer on the titanate nanobelt surface. When the sample was calcined at 450 °C, the temperature at which a $Bi_{20}TiO_{32}$ surface layer was produced (Fig. 1), it can be seen that the nanobelts again displayed smooth and clean surfaces, with the width of the nanobelts being 100–250 nm, the thickness being 30–50 nm and the length being up to several tens of micrometers, as shown in panel (b). Note that the average length and width of these TiO_2(B)@$Bi_{20}TiO_{32}$ core–shell nanobelts were slightly greater than those of pure TiO_2(B) nanobelts prepared by similar calcination but without bismuth modification (Fig. S2b). When the calcination temperature was increased to 600 °C in panel (c) and 700 °C in panel (d), the nanobelt morphology exhibited no obvious difference,

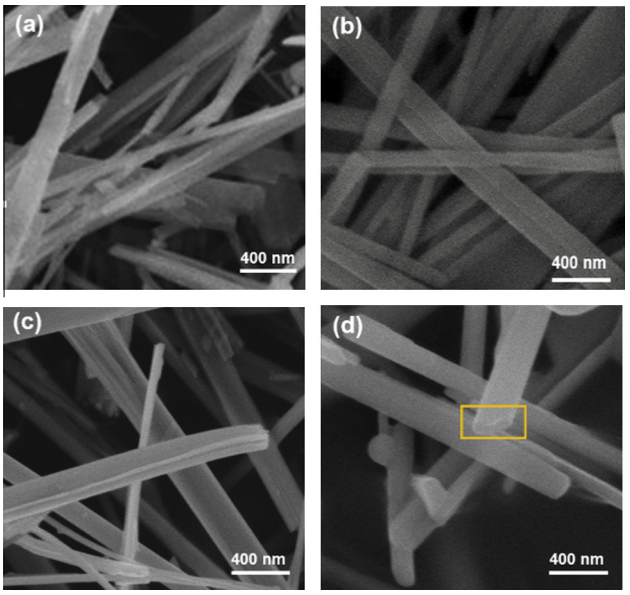

Fig. 4. Representative SEM images of the hybrid nanobelts calcined at different temperatures: (a) as prepared, (b) 450 °C, (c) 600 °C and (d) 700 °C. The scale bars are all 400 nm.

indicating good thermal stability. However, at 700 °C, at which temperature the nanobelts were transformed completely to $Bi_4Ti_3O_{12}$ although the belt-like morphology was preserved, one can see a number of bulges on the surface of the nanobelts (highlighted by the orange rectangle), and some sintered necks at the contact points between nanobelts (Fig. 4d).

HRTEM studies were then employed to further investigate the morphology and microstructures of the nanobelt samples. For the TiO_2(B)@$Bi_{20}TiO_{32}$ nanobelts prepared by calcination at 450 °C (Fig. 5a), the width of the nanobelts can be estimated to be in the range of 100–250 nm and the length up to several tens of micrometers, consistent with the SEM results shown in Fig. 4. Additionally, along the long-axis direction, one low-contrast strip can be seen on each side of the center part of the nanobelts, indicating the formation of a core–shell nanostructure with two different crystalline phases. In fact, scanning transmission electron microscopic measurements showed different chemical compositions between the central and side parts of the nanobelts, as manifested in the dark-field image of Fig. 5b, where the outside parts of the nanobelt were identified as $Bi_{20}TiO_{32}$ and the central part TiO_2(B). That is, the nanobelts prepared by calcination at 450 °C exhibited a unique TiO_2(B)@$Bi_{20}TiO_{32}$ core–shell structure. The width

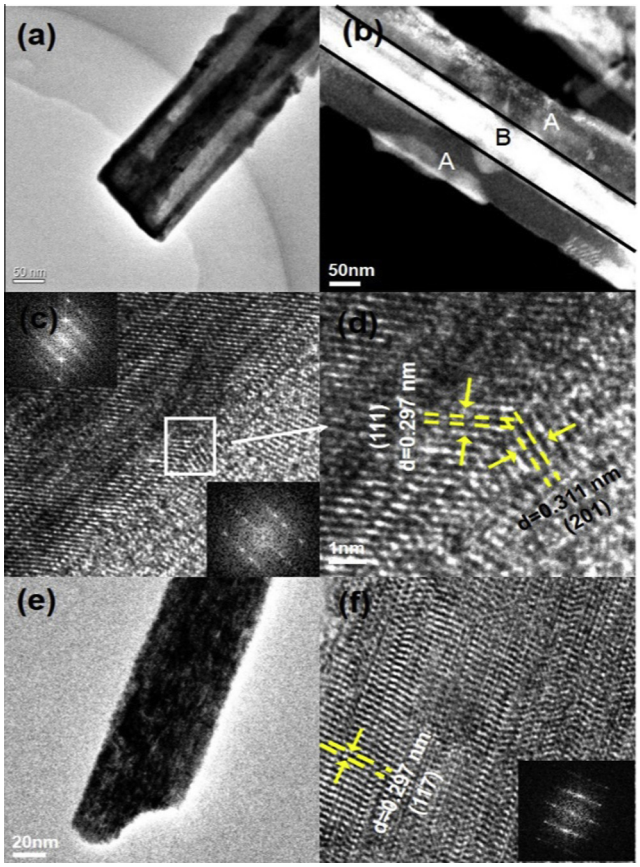

Fig. 5. Representative (HR)TEM images of (a–d) TiO_2(B)@$Bi_{20}TiO_{32}$ nanobelts that were prepared by calcination at 450 °C and (e, f) $Bi_4Ti_3O_{12}$ nanobelts that were prepared by calcination at 700 °C.

of the TiO_2(B) core and the $Bi_{20}TiO_{32}$ shell was about 50 and 60 nm, respectively. The detailed structures were highlighted by high–resolution imaging in panels (c) and (d). It can be seen that the crystal lattice directions of the two phases are different, with an obvious interface. The insets to Fig. 5c are the Fourier-transformed patterns of these two phases, showing that both regions were single crystalline. Fig. 5d is a high-resolution image of the selected area signified by the white square in panel (c), where a high degree of crystallinity of the two phases can be clearly seen. The lattice fringes of TiO_2(B) and $Bi_{20}TiO_{32}$ can be identified with a spacing of 0.297 and 0.311 nm, respectively, corresponding to the (1 1 1) planes of TiO_2(B) and (2 0 1) of $Bi_{20}TiO_{32}$.

For the nanobelts prepared by calcination at 700 °C (Fig. 5e), the sample appeared to exhibit a rather homogeneous image contrast, suggesting the formation of a uniform crystalline phase throughout the entire nanobelts. This is consistent with the XRD measurements in Fig. 1, which show that the nanobelts were converted to single-crystalline $Bi_4Ti_3O_{12}$. This is likely because of interfacial diffusion of bismuth cations from the outer layer into the central part. Fig. 5f depicts the HRTEM image of a nanobelt calcinated at 700 °C. The spacing of the lattice fringes was estimated to be 0.297 nm, consistent with the (1 1 7) planes of $Bi_4Ti_3O_{12}$. The corresponding Fourier-transformed patterns (inset to panel f) also confirmed that the resulting $Bi_4Ti_3O_{12}$ nanobelts were highly crystalline.

On the basis of the above experimental observations, the phase transformation of the nanobelts might be accounted for by the following mechanism, as shown in Fig. 6. Note that in water $Bi(NO_3)_3$ might undergo a hydrolysis reaction:

$$Bi(NO_3)_3 + H_2O \rightarrow BiONO_3 + HNO_3 \quad (1)$$

forming $BiONO_3$ nanoparticles under ultrasonic irradiation. As a by-product, HNO_3 was also produced, which lowered the pH of the solution [31]. When the sodium titanate nanobelts were immersed into the $Bi(NO_3)_3$ solution, Na^+ ions in the interlayers of the $Na_2Ti_3O_7$ nanobelts might be substituted by H^+, leading to the formation of $H_2Ti_3O_7$ nanobelts [22],

$$Na_2Ti_3O_7 + H^+ \rightarrow H_2Ti_3O_7 + Na^+ \quad (2)$$

This ion replacement reaction was likely facilitated by the layered structure of the sodium titanate nanobelts, which includes corner- and edge-shared Ti–O octahedra and sodium ions sandwiched between two TiO_6 octahedron layers (Fig. 6a and b). Note also that the radius of hydrated hydrogen ions (0.135 nm) is markedly smaller than that of hydrated sodium ions (0.36 nm) [32]. In fact, the ion-exchange reaction (Fig. 6c) can be manifested by the apparent change of the Na^+ concentration after the nanobelts were immersed in the $Bi(NO_3)_3$ solution. For instance, when $Na_2Ti_3O_7$ nanobelts (550 mg) were added to a 0.05 M $Bi(NO_3)_3$ solution and mixed for 48 h, the concentration of sodium ions in the water solution was

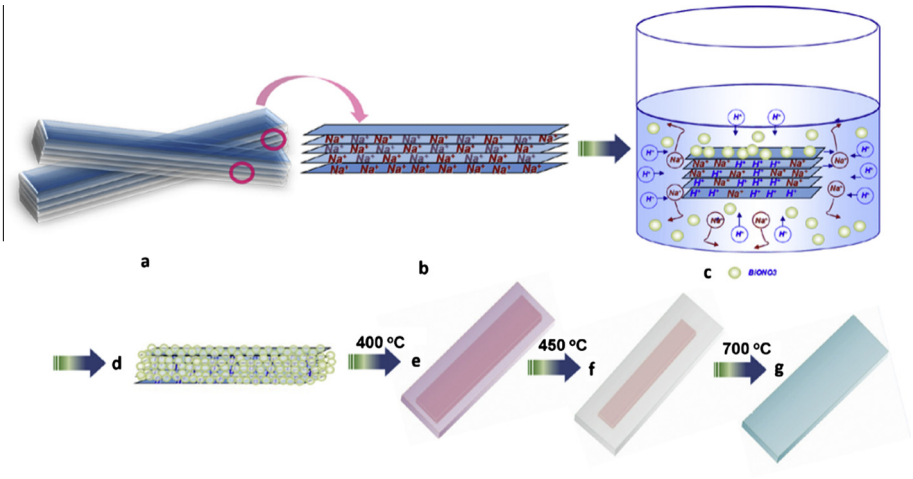

Fig. 6. Schematic of the reaction and phase transformation mechanism of bismuth titanate nanobelts.

found to increase from zero to 80.80 ppm, as determined by inductively coupled plasma mass spectrometric measurements. In comparison, when the $Na_2Ti_3O_7$ nanobelts were immersed into pure water, only 0.23 ppm of Na^+ was detected under otherwise identical conditions (Table S1).

In this process, the assembly of $BiONO_3$ onto $H_2Ti_3O_7$ was likely driven by electrostatic interactions, as zeta potential measurements showed that the $H_2Ti_3O_7$ nanobelts were positively charged at 35.4 ± 1.2 mV and $BiONO_3$ nanoparticles were negatively charged at -10.3 ± 3.5 mV (Table S2), leading to the formation of $H_2Ti_3O_7$@$BiONO_3$ core–shell nanobelts (Fig. 6d). Note that in this process $Na_2Ti_3O_7$ functioned not only as the reactant but also as the template. When these Bi-modified nanobelts were subject to calcination at controlled temperatures, the $BiONO_3$ nanoparticle layer was then converted to Bi_2O_3 and the interior $H_2Ti_3O_7$ to TiO_2(B) at 450 °C:

$$BiONO_3 \rightarrow Bi_2O_3 + N_xO_y \quad (3)$$

$$H_2Ti_3O_7 \rightarrow 3TiO_2(B) + H_2O \quad (4)$$

That is, a Bi_2O_3 layer was formed on the surface of TiO_2(B) nanobelts, resulting in TiO_2(B)@Bi_2O_3 core–shell hybrid nanobelts (Fig. 6e). As $H_2Ti_3O_7$ and TiO_2(B) possess the same monoclinic crystal structure with similar lattice parameters along the *c*-axis, there was likely a low energy barrier involved in the transformation of $H_2Ti_3O_7$ to TiO_2(B) nanobelts [27].

In a control experiment with pure $BiONO_3$ nanoparticles, XRD studies showed that, when heated at 450 °C, $BiONO_3$ was converted to $Bi_5O_7NO_3$ but not to Bi_2O_3 (Fig. S3). Only when the calcination temperature was increased to 600 °C did Bi_2O_3 start to appear as a decomposition product. The relevant DTA/TG data of $BiONO_3$ agreed with the XRD results (Fig. S4), where the exothermic peak for Bi_2O_3 was identified at 505 °C. For the $BiONO_3$ nanoparticles supported on the TiO_2(B) surface, a much lower decomposition temperature was observed, likely because of the small thickness. Therefore, Bi_2O_3 nanoparticles were formed on the surface of TiO_2(B) nanobelts even at only 450 °C (Fig. 1). In fact, energy-dispersive X-ray spectroscopy (EDS) analysis of the nanobelts heated at 450 °C (Fig. S5) detected no N element, indicating that $BiONO_3$ was decomposed to Bi_2O_3 completely. At increasing calcination temperatures, Bi_2O_3 diffused into the TiO_2 (B) nanobelts, where the mixing of TiO_2(B) and Bi_2O_3 led to the formation of a $Bi_{20}TiO_{32}$ metastable phase. Since the content of TiO_2(B) was in large excess compared to that of Bi_2O_3, there was residual TiO_2(B) in the center of the nanobelts at 450 °C, thereby forming core–shell TiO_2 (B)@$Bi_{20}TiO_{32}$ nanobelts (Fig. 6f). At even higher temperatures, the equilibrium with the metastable phase was broken and new solid-phase reactions occurred, eventually leading to the formation of $Bi_4Ti_3O_{12}$ as the sole products (Fig. 6g). The key steps of the reactions may be summarized as:

$$10Bi_2O_3 + TiO_2 \rightarrow Bi_{20}TiO_{32} \quad (5)$$

$$Bi_{20}TiO_{32} + 14TiO_2 \rightarrow 5Bi_4Ti_3O_{12} \quad (6)$$

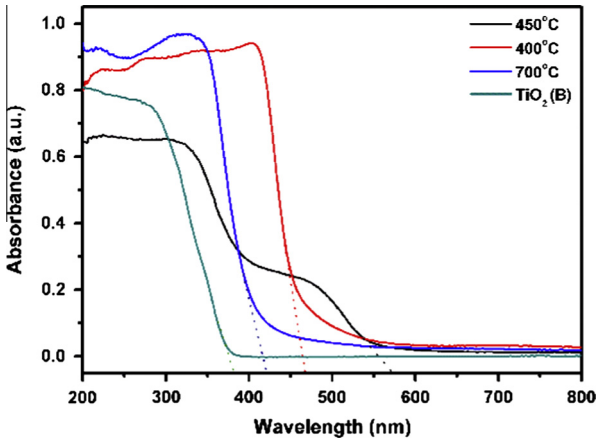

Fig. 7. UV–vis DRS spectra of TiO_2(B) nanobelts before and after being calcined at 400, 450 and 700 °C.

The electronic structures of the above-obtained nanobelts were then examined by spectroscopic measurements. Fig. 7 shows the UV–vis absorption spectra of the TiO_2(B), TiO_2(B)@Bi_2O_3, TiO_2(B)@$Bi_{20}TiO_{32}$ and $Bi_4Ti_3O_{12}$ nanobelts. The absorption edge can be estimated to be 380, 455, 570 and 420 nm, respectively. This corresponds to an effective band gap energy of 3.20, 2.71, 2.36 and 3.00 eV, respectively. That is, among the series, TiO_2(B)@$Bi_{20}TiO_{32}$ nanobelts exhibited the smallest band gap, which means the widest range of light absorption among the series in the generation of the charge carriers. Note that the band structures play an important role in the determination of the photocatalytic property [33,34]. The conduction band (CB) and VB potentials of a semiconductor at the point of zero charge can be calculated by using the following empirical equation [35],

$$E_{CB} = X - E_e - 0.5E_g \quad (7)$$

where E_{CB} denotes the conduction band edge potential, X is the geometric mean of the Mulliken electronegativity of the constituent atoms, E_e is the energy of free electrons on the hydrogen scale (about 4.5 eV) and E_g is the band gap. As the X factors for TiO_2(B), Bi_2O_3, $Bi_{20}TiO_{32}$ and $Bi_4Ti_3O_{12}$ are about 5.81, 6.23, 5.91 and 4.12 eV [35], respectively, the corresponding VB edge potential can be determined to be +2.91, +3.09, +2.59 and +1.12 eV. These results are depicted in Fig. 8.

PL spectroscopic studies were then carried out to evaluate the separation and recombination of photogenerated electrons and holes. The PL spectra of TiO_2(B) nanobelts, Bi_2O_3 nanoparticles, TiO_2(B)@$Bi_{20}TiO_{32}$ nanobelts and $Bi_4Ti_3O_{12}$ nanobelts are shown in Fig. 9. At the excitation wavelength of 300 nm, the TiO_2(B) nanobelts (black curve) displayed two strong emission peaks at about 400 and 470 nm, which might be attributed to the emission of the band gap transition and that of the charge transfer transition of oxygen vacancy-trapped electrons, respectively. Similar features were also observed with the TiO_2(B)@$Bi_{20}TiO_{32}$ (blue curve) and $Bi_4Ti_3O_{12}$ (green curve) nanobelts, but with markedly lower PL intensity. In contrast, Bi_2O_3 nanoparticles (red curve) showed a single emission peak at around 470 nm, which is likely due to the intrinsic luminescence. Notably, among the series, the TiO_2(B)@$Bi_{20}TiO_{32}$ nanobelts (blue curve) exhibited the lowest PL emission intensity. It is likely that the photo-excited electrons transfer from the CB band of TiO_2(B) core to the CB band of the $Bi_{20}TiO_{32}$ shell (Fig. 8), leading to effective PL quenching.

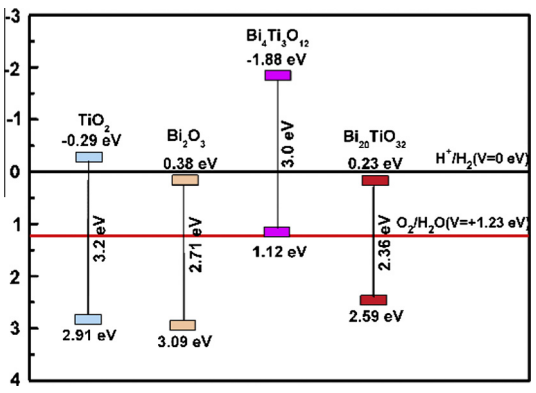

Fig. 8. Schematic diagram of the band structures of TiO_2(B), Bi_2O_3, $Bi_{20}TiO_{32}$ and $Bi_4Ti_3O_{12}$ nanobelts.

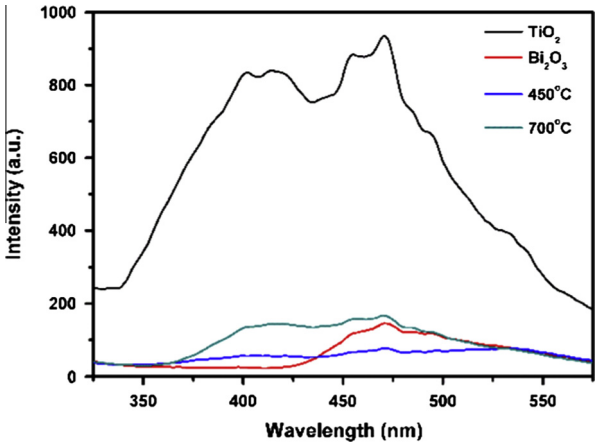

Fig. 9. PL spectra of TiO_2(B) nanobelts, Bi_2O_3 nanoparticles, TiO_2(B)@$Bi_{20}TiO_{32}$ (450 °C) and $Bi_4Ti_3O_{12}$ (700 °C) nanobelts. The excitation wavelength was set at 300 nm.

Such unique band structures of the hybrid nanobelts might be exploited for photocatalytic applications. MO was chosen as a model organic pollutant under UV irradiation to evaluate the photocatalytic activity. The ratio of the difference between the initial absorption intensity and the residual intensity at a certain reaction time of the MO solution ($C_0 - C_t$) divided by the initial absorption intensity (C_0) represents the degree of degradation. Fig. 10a shows the photocatalytic degradation of MO in water as a function of irradiation time under UV light in the absence and presence of TiO_2(B) nanobelts, TiO_2(B)@Bi_2O_3 nanobelts, TiO_2(B)@$Bi_{20}TiO_{32}$ and $Bi_4Ti_3O_{12}$ nanobelts. The adsorbed amounts of MO within 20 min in the dark for all nanobelts are less than 20%. From Fig. 10a, it can be seen that, without the addition of a catalyst, MO could not be decomposed under UV irradiation. After UV exposure for 50 min, about 96.89% and 77.29% of MO were degraded by the TiO_2(B)@$Bi_{20}TiO_{32}$ and $Bi_4Ti_3O_{12}$ samples, respectively. In contrast, only 47.23% and 30.87% of MO were degraded by the TiO_2(B)@Bi_2O_3 and TiO_2(B) nanobelts. The results are consistent with the DRS data, and demonstrate that a heterostructure involved in the TiO_2(B)@$Bi_{20}TiO_{32}$ core–shell nanobelts might enhance the separation of photoinduced carriers, leading to improved photocatalytic performance.

To investigate the stability of the TiO_2(B)@$Bi_{20}TiO_{32}$ core–shell nanobelts in photocatalysis under UV light irradiation, the same samples were repeatedly used eight times after separation via membrane filtration, and the results are shown in Fig. 10b. Only a small decrease was observed of the photocatalytic activity by the TiO_2(B)@$Bi_{20}TiO_{32}$

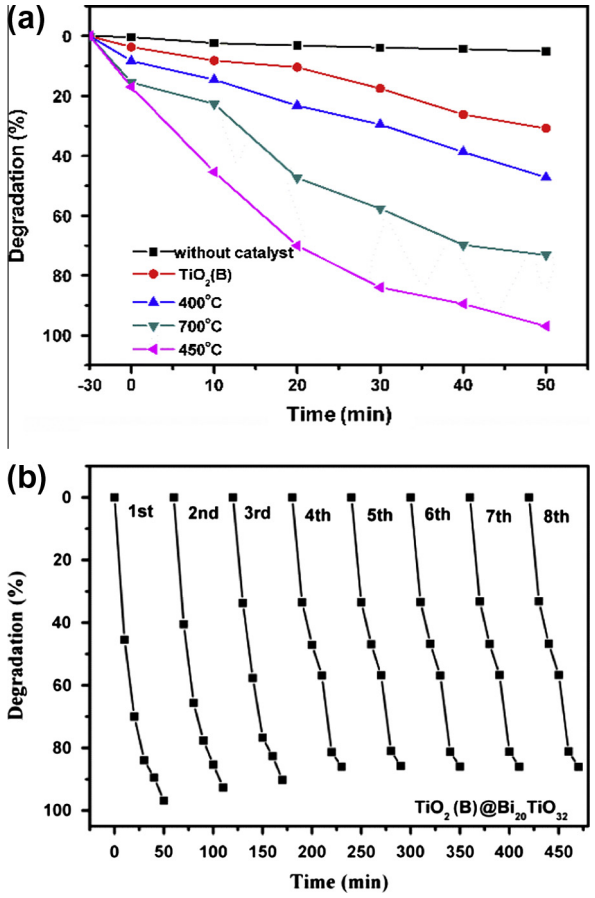

Fig. 10. (a) Photocatalytic decomposition activity of the as-prepared TiO_2(B) nanobelts and those calcined at 400, 450 and 700 °C under UV light irradiation; and (b) the photocatalytic stability of the sample calcined at 450 °C.

nanobelts after eight cycles. For instance, after 50 min of photoirradiation, the total amount of MO that was degraded was 96.89% in the first run, 92.65% in the second, 90.23% in the third, 86.02% in the fourth and remained virtually unchanged thereafter. This indicates good structural stability under UV irradiation for the phototcatalytic decomposition of organic pollutants.

4. Conclusions

A facile method was developed, for the first time, for the synthesis of bismuth titanate nanobelts by the assembly of a $BiONO_3$ layer on $H_2Ti_3O_7$ nanobelt surfaces followed by a calcination process. $BiONO_3$ nanoparticles were formed by the hydrolysis of $Bi(NO_3)_3$, which adsorbed onto the titanate nanobelt surfaces by electrostatic interactions. The resulting $H_2Ti_3O_7$@$BiONO_3$ bismuth titanate nanobelts were then subject to a calcination treatment at controlled temperatures. At the low calcination temperature of 400 °C, TiO_2(B)@Bi_2O_3 hybrid nanobelts were obtained. At the higher temperature of 450 °C the hybrid nanobelts were converted into TiO_2(B)@$Bi_{20}TiO_{32}$ through interfacial ion diffusion and nanoscale solid-state reactions. With a further increase in the calcination temperature to 600–700 °C, solid-state reactions between the TiO_2(B) core and the $Bi_{20}TiO_{32}$ shell took place, forming a single-phase nanobelt structure of $Bi_4Ti_3O_{12}$. Interestingly, within the present experimental context, the hybrid nanobelts with a core–shell nanostructure exhibited enhanced photocatalytic ability as compared with pure TiO_2(B) or Bi_2O_3 nanoparticles, and the TiO_2(B)@$Bi_{20}TiO_{32}$ core–shell nanobelts stood out as the optimal catalysts among the series, likely because of a preferred orientation to form well-matched and stable phase interfaces via self-transformation such that the photo-excited electrons might transfer from the CB band of TiO_2(B) core to the CB band of the $Bi_{20}TiO_{32}$ shell, as manifested in the effective quenching of the nanobelt photoluminescence.

Acknowledgements

This research was supported by National Natural Science Foundation of China (NSFDYS: 50925205, 51002089 Innovation Research Group IRG 51021062), the Program of Introducing Talents of Discipline to Universities in China (111 Program b06015) and the "100 Talents Program" of Chinese Academy of Sciences.

Appendix A. Supplementary data

XRD patterns of $Na_2Ti_3O_7$ nanobelts, representative SEM images of $Na_2Ti_3O_7$ nanobelts and pure TiO_2 nanobelts, concentrations of Na^+ ions before and after the immersion of the nanobelts in $BiONO_3$ suspension or ultrapure water, zeta potentials of $BiONO_3$ and $H_2Ti_3O_7$ suspension, XRD patterns of $BiONO_3$ sintered at 450 and 600 °C, DTA/TG curves of $BiONO_3$ and EDS spectrum of precursor heated at 450 °C. Supplementary data associated with this article can be found, in the online version, at http://dx.doi.org/10.1016/j.actamat.2013.10.006.

References

[1] Cummins S, Cross L. J Appl Phys 1968;39:2268.
[2] Yordanov S, Ivanov I, Carapanov CP. J Phys D: Appl Phys 1998;31:800.
[3] Petrov M, Sochava S, Stepanov S. Opt Lett 1989;14:284.
[4] Yang X, Huang B, Wang H, Shang S, Yao W, Wei J. J Cryst Growth 2004;270:98.
[5] Lin X, Lv P, Guan Q, Li H, Zhai H, Liu C. Appl Surf Sci 2012;258:7146.
[6] Cheng H, Huang B, Dai Y, Qin X, Zhang X, Wang Z, et al. J Solid State Chem 2009;182:2274.
[7] Radosavljevic I, Evans J, Sleight A. J Solid State Chem 1998;136:63.
[8] Rao A, Robin A, Komarneni S. Mater Lett 1996;28:469.
[9] Toyoda M, Hamaji Y, Tomono K, Payne DA. Jpn J Appl Phys 1993;32:4158.
[10] Yang Q, Li Y, Yin Q, Wang P, Cheng Y-B. J Eur Ceram Soc 2003;23:161.
[11] Yao WF, Wang H, Xu XH, Shang SX, Hou Y, Zhang Y, et al. Mater Lett 2003;57:1899.
[12] Wu N, Wang J, Tafen DN, Wang H, Zheng J-G, Lewis JP, et al. J Am Chem Soc 2010;132:6679.

[13] Liu Y, Zhong L, Peng Z, Cai Y, Song Y, Chen W. CrystEngComm 2011;13:5467.
[14] Piccinini M, Ntainjua E, Edwards JK, Carley AF, Moulijn JA, Hutchings GJ. Phys Chem Chem Phys 2010;12:2488.
[15] Zhang F, Jin R, Chen J, Shao C, Gao W, Li L, et al. J Catal 2005;232:424.
[16] Xin B, Jing L, Ren Z, Wang B, Fu H. J Phys Chem B 2005;109:2805.
[17] Lin J, Shen J, Wang R, Cui J, Zhou W, Hu P, et al. J Mater Chem 2011;21:5106.
[18] Tian J, Sang Y, Yu G, Jiang H, Mu X, Liu H. Adv Mater 2013;25:5075–80.
[19] Zhou W, Liu H, Wang J, Liu D, Du G, Cui J. ACS Appl Mater Interfaces 2010;2:2385.
[20] Zhao Z, Tian J, Wang D, Kang X, Sang Y, Liu H, et al. J Mater Chem 2012;22:23395.
[21] Priya R, Baiju K, Shukla S, Biju S, Reddy M, Patil K, et al. Catal Lett 2009;128:137.
[22] Wang Y, Du G, Liu H, Liu D, Qin S, Wang N, et al. Adv Funct Mater 2008;18:1131.
[23] Zhou W, Du G, Hu P, Yin Y, Li J, Yu J, et al. J Hazard Mater 2011;197:19.
[24] Zhou T, Hu J. Environ Sci Technol 2010;44:8698.
[25] Hou Y, Wang M, Xu X, Wang H, Shang S, Wang D, et al. J Cryst Growth 2002;240:489.
[26] Wang F, Wang J, Zhong X, Li B, Liu J, Wu D, et al. CrystEngComm 2013;15:1397.
[27] Zhou W, Gai L, Hu P, Cui J, Liu X, Wang D, et al. CrystEngComm 2011;13:6643.
[28] Durán P, Capel F, Moure C, Villegas M, Fernández JF, Tartaj J, et al. J Eur Ceram Soc 2001;21:1.
[29] Jiang T, Xu K, Ji S. J Chem Soc Faraday Trans 1996;92:3401.
[30] Chen Z, Yu Y, Hu J, Shui A, He X. Hydrothermal synthesis and characterization of $Bi_4Ti_3O_{12}$ powders. J Ceram Soc Jpn 2009;117:264.
[31] Zhou S, Li J, Ke Y, Lu S. Mater Lett 2003;57:2602.
[32] Ren N, Li R, Chen L, Wang G, Liu D, Wang Y, et al. J Mater Chem 2012;22:19151.
[33] Zeng J, Wang H, Zhang Y, Zhu MK, Yan H. J Phys Chem C 2007;111:11879.
[34] Wang P, Huang B, Zhang X, Qin X, Dai Y, Jin H, et al. Chem Eur J 2008;14:10543.
[35] Nethercot AH. Phys Rev Lett 1974;33:1088.